

Structural mechanism of voltage-dependent gating in an isolated voltage-sensing domain

Qufei Li¹, Sherry Wanderling¹, Marcin Paduch¹, David Medovoy¹, Abhishek Singharoy², Ryan McGreevy², Carlos A Villalba-Galea³, Raymond E Hulse¹, Benoît Roux^{1,4}, Klaus Schulten^{2,5}, Anthony Kossiakoff^{1,4} & Eduardo Perozo^{1,4}

The transduction of transmembrane electric fields into protein motion has an essential role in the generation and propagation of cellular signals. Voltage-sensing domains (VSDs) carry out these functions through reorientations of positive charges in the S4 helix. Here, we determined crystal structures of the *Ciona intestinalis* VSD (Ci-VSD) in putatively active and resting conformations. S4 undergoes an ~5-Å displacement along its main axis, accompanied by an ~60° rotation. This movement is stabilized by an exchange in countercharge partners in helices S1 and S3 that generates an estimated net charge transfer of ~1 e₀. Gating charges move relative to a 'hydrophobic gasket' that electrically divides intra- and extracellular compartments. EPR spectroscopy confirms the limited nature of S4 movement in a membrane environment. These results provide an explicit mechanism for voltage sensing and set the basis for electromechanical coupling in voltage-dependent enzymes and ion channels.

Electrical excitability derived from voltage-dependent ion channels is a fundamental biological phenomenon that underlies key physiological events, including cellular communication, information coding, motility and sensation. Few mechanisms can endow a membrane protein with the ability to respond to changes in the transmembrane electric field. As predicted in an early study¹, these mechanisms are associated with the reorientation of a set of fixed charges (or dipoles) that respond to changes in transmembrane voltage. Indeed, the rearrangement of these fixed charges has been measured experimentally as a nonlinear capacitive current (the gating or sensing current)²—an electrical expression of the conformational changes associated with the activation of the voltage sensor.

Initial examination of the first amino acid sequence of voltage-gated channels suggested that they were assembled from two separate domains: a VSD comprising four transmembrane helices (S1–S4) and a pore domain (helices S5 and S6) responsible for gate opening and ion selectivity^{3–5}. In most voltage-gated channels, the S4 segment is decorated with four to eight basic amino acids (mostly arginines), a fact that made it a logical candidate to fulfill the requirements of the voltage sensor. Extensive site-directed mutagenesis experiments convincingly demonstrated the role of these S4 charges in sensing voltage^{6,7}. Evidence that the S4 physically moves in response to voltage changes came from a series of insightful experiments based on the reactivity of cysteine mutants to sulfhydryl-based chemical labels^{8,9} and voltage-clamp fluorometry measurements^{10,11}.

The mechanism of voltage sensing in excitable cells remains one of the most challenging subjects in modern biophysics. Yet, in spite of a great deal of progress derived from multidisciplinary approaches,

defining this mechanism still requires high-resolution structures of VSDs in both the activated (up) and resting (down) conformations. Crystal structures of the voltage-dependent K⁺ channels KvAP¹² and Kv1.2 (refs. 13,14) and two prokaryotic Na⁺ channels^{15,16} have clarified many of the basic concepts regarding the architecture of the VSD and its associated pore domain. On the basis of their voltage dependences, not surprisingly, these VSDs all appear to populate the same up-state conformation at 0 mV in the absence of an electric field at the crystal conditions. The down conformation has been vigorously pursued but has remained structurally unattainable.

The recent discoveries of voltage-sensing phosphatases (VSP)¹⁷ and voltage-gated proton channels (Hv1)^{18,19} have revealed that VSDs are not exclusive to ion channels with canonical pore domains but can operate as independent functional domains. The voltage-sensitive phosphatase from *C. intestinalis* (Ci-VSP) has a PTEN-related phosphoinositide phosphatase²⁰ that is controlled by a standard VSD with high sequence similarity to the S1–S4 segments found in Na⁺ and K⁺ channels (Fig. 1a). To address the fundamental questions regarding how membrane proteins sense transmembrane voltages, we set out to determine the structure of a VSD under conditions that stabilize both the up and the down conformations in the same experimental system. To this end, we have focused our attention on Ci-VSD, the VSD of Ci-VSP in the absence of its phosphatase.

RESULTS

Manipulating the conformational landscape of Ci-VSD at 0 mV

When expressed in *Xenopus* oocytes, Ci-VSP produced nonlinear capacitive currents (Fig. 1b) similar to those previously observed in

¹Department of Biochemistry and Molecular Biology, University of Chicago, Chicago, Illinois, USA. ²Beckman Institute, University of Illinois at Urbana-Champaign, Urbana, Illinois, USA. ³Department of Physiology and Biophysics, Virginia Commonwealth University School of Medicine, Richmond, Virginia, USA. ⁴Institute of Biophysical Dynamics, University of Chicago, Chicago, Illinois, USA. ⁵Department of Physics, University of Illinois at Urbana-Champaign, Urbana, Illinois, USA. Correspondence should be addressed to E.P. (eperozo@uchicago.edu).

Received 21 October 2013; accepted 10 January 2014; published online 2 February 2014; corrected online 23 February 2014 (details online); doi:10.1038/nsmb.2768

Figure 1 Stabilizing two conformations of Ci-VSD by local field engineering. **(a)** Ci-VSP is composed of a voltage sensing domain and a phosphatase domain. Left, linear schematics of Ci-VSP sequence regions. Highlighted in red is the conserved S4 helix containing positive charges every three residues. The relative location of the protein constructs for crystallization is shown on top: residues 89–260 (1) for R217E mutant and 106–244 (2) for WT. Ch, chimera. Right, general cartoon of Ci-VSD embedded in a lipid membrane. **(b)** Representative traces ($n = 5$) of Ci-VSP gating currents. $V_{1/2}$ is +58 mV for WT (black circles), –15 mV for R217Q (white triangles) and –62 mV for R217E (red triangles). Under <0 mV conditions, Ci-VSD populates the activated (up) state for the R217E mutant and the resting (down) state for WT. **(c)** Positive holding potential can promote transition of VSDs into relaxed state that generates a leftward shift of its voltage dependence. Left, basic kinetic cycle of canonical gating transitions. Right, plot (error bars are s.d., $n = 5$) showing voltage dependence of the transition into the relaxed state in the presence of a steady-state prepulse.

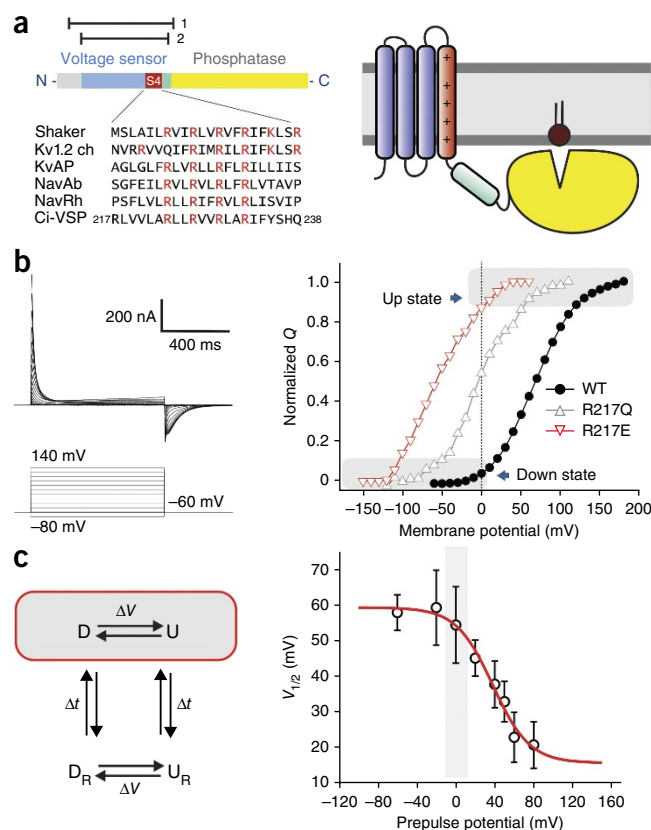
voltage-gated channels^{17,21}, and this behavior was fully recapitulated by the sensor alone^{22,23}. Yet, in comparison to VSDs from ion channels, the Ci-VSP's charge-voltage (Q - V) curve is greatly shifted to more positive potentials, with a half-maximal voltage ($V_{1/2}$) near +60 mV (ref. 17) (**Fig. 1b**). A fortunate consequence of a shifted Q - V curve is that, in the absence of a membrane potential, Ci-VSD should stably populate the down conformation of the voltage sensor at 0 mV. Furthermore, the Q - V curve of Ci-VSP can be easily shifted left by neutralization of a basic residue at position 217 (refs. 23,24) (**Fig. 1b**). Addition of an acidic residue (R217E)²⁵ generates a negative shift of ~120 mV in the hyperpolarizing direction ($V_{1/2}$ near –60 mV) and provides a straightforward strategy to stabilize the Ci-VSD up conformation, also at 0 mV (**Fig. 1b**).

However, when exposed to long-term depolarization, VSDs transition to new 'relaxed' conformations of the up and down states (U_R , D_R)²². In these states, the voltage dependence is sharply shifted toward negative potentials as a result of changes in the kinetics of charge return. Therefore, transitions to relaxed states occur in parallel to the standard voltage-driven $D \leftrightarrow U$ equilibrium, according to a simple kinetic cycle (**Fig. 1c**)²². We wondered whether the long-term influence of 0-mV conditions would stabilize the relaxed states in Ci-VSD in our biochemical sample and determined the dependence of a steady-state prepulse on the $V_{1/2}$ of the Q - V curve (**Fig. 1c**). The results indicated that the transition to the relaxed states appeared to take place at only large positive potentials. These results highlight the fact that the engineering of a local field through one particular residue in Ci-VSD allows the study of its canonical ($D \leftrightarrow U$) structural rearrangements at 0 mV.

Structure of Ci-VSD in its activated conformation

We crystallized *Escherichia coli*-expressed²⁶ Ci-VSD in complex with synthetic Fab as a crystallization chaperone, as previously described²⁷. Ci-VSD R217E in complex with Fab 33F12_4 from two distinct crystallization conditions generated crystals that diffracted to resolutions of 2.5 and 2.8 Å (**Table 1** and **Supplementary Fig. 1a–c**). We solved the essentially identical structures with different water molecules inside the voltage sensor by molecular replacement, using the Fab molecule, and refined them to $R_{\text{work}}/R_{\text{free}}$ of 20.0/24.0 (2.5-Å data) and 21.2/26.4 (2.8-Å data). The Fab binds to an epitope formed by the S3-S4 loop and the top of S4 (**Supplementary Fig. 1b**). We observed the head groups of three detergent molecules and a solvent molecule in the vicinity of the S3-S4 loop (**Supplementary Fig. 1d**), results consistent with the hydrophilic environment anticipated around the extracellular surface.

The Ci-VSD R217E is arranged as an antiparallel four-helix bundle (**Fig. 2a**), in agreement with the basic three-dimensional architecture



of all known VSDs^{12,14–16}. S1 is preceded by a short 3.5-turn amphipathic helix S0, and it is likely to be oriented parallel to the plane of the membrane. The relative alignment of helices S1–S4 sets up a fairly large water-filled extracellular cavity and a smaller opening on the intracellular side (**Fig. 2b**). There are a total of five charges in Ci-VSD's S4 helix. The topmost, R217 (mutated to glutamate in this structure), points straight away from the outer vestibule and presumably engages in direct interactions with the lipid head groups. Electrophysiological evidence suggests that R217 does not contribute to charge transfer²⁸, so we refer to it as R0. The putative gating charges are thus R223 (R1), R226 (R2), R229 (R3) and R232 (R4). The four gating charges appear to be stabilized by a combination of hydrogen-bonding and direct electrostatic ion pairing. R1 and R2 are in a fully extended rotameric conformation, pointing straight toward the extracellular vestibule (**Fig. 2a**). From the two R217E structures, we identified five crystallographic waters in the external cavity, with two of them establishing hydrogen-bonding interactions with R1 (**Fig. 2d**). There are only three obvious countercharges: D129 in S1 (D1) and D186 and E183 in S3 (D2 and E3, respectively). R2 is within 4.6 Å of D1 and is simultaneously in range for hydrogen-bonding with two waters (**Fig. 2c,d**). R3 is located well within range (4.6 Å) of ion-pair interactions with D2, whereas R4 appears neatly intertwined between D2 and E3 (4.3 Å and 4.6 Å, respectively). Surprisingly, and despite the strong sequence and structural conservation with VSDs in K^+ and Na^+ channels, we see no viable countercharges in S2 of Ci-VSD, a result that points to an interesting heterogeneity in the way in which gating charges might traverse the transmembrane electric field in other VSDs.

In spite of being located on a standard α -helix, the slight bend and tilt of S4 place all four gating arginines along a remarkably straight line (**Fig. 2c**). We argue that this has important implications regarding the potential mechanism of charge transfer, because the aligned

Table 1 Data collection and refinement statistics

| | R217E-33F12_4 | 217E-33F12_4 | WT-39D10_18 |
|---|---------------------------------|----------------------------|--------------------------|
| Data collection | | | |
| Space group | <i>P</i> 6 ₅ 22 | <i>P</i> 6 ₅ 22 | <i>P</i> 1 |
| Cell dimensions | | | |
| a, b, c (Å) | 121, 121, 230 | 121, 121, 230 | 77.3, 94.2, 193.9 |
| α, β, γ (°) | 90, 90, 120 | 90, 90, 120 | 102.6, 93.5, 105.3 |
| Resolution (Å) | 50–2.5 (2.66–2.52) ^a | 50–2.8 (2.85–2.80) | 50–3.6 (3.66–3.60) |
| <i>R</i> _{sym} | 16.8 (134.7) | 16.8 (95.8) | 14.4 (87.1) ^b |
| <i>I</i> / σ <i>I</i> | 8.2 (2.0) | 9.2 (2.2) | 12.2 (1.0) |
| Completeness (%) | 99.8 (100) | 100 (100) | 95.1 (83.2) |
| Redundancy | 5.1 (5.3) | 8.2 (7.2) | 2.9 (2.2) |
| Refinement | | | |
| Resolution (Å) | 38.6–2.5 | 37.4–2.8 | 50–3.6 |
| No. reflections | 33,756 | 24,429 | 55,790 |
| <i>R</i> _{work} / <i>R</i> _{free} | 0.17 / 0.24 | 0.21 / 0.26 | 0.25 / 0.29 |
| No. atoms | | | |
| Protein | 4,303 | 4,262 | 17,446 |
| Ligand/ion | 153 / 1 | 16 / 2 | |
| Water | 197 | 35 | |
| <i>B</i> factors (Å ²) | | | |
| Protein | 48 | 54 | 150 |
| Ligand/ion | 39 / 32 | 48 / 44 | |
| Water | 41 | 39 | |
| r.m.s. deviations | | | |
| Bond lengths (Å) | 0.011 | 0.011 | 0.005 ^d |
| Bond angles (°) | 1.316 | 1.338 | 0.38 ^e |

^aValues in parenthesis are for the highest-resolution shell. ^bWT data were merged with 348 selected frames from eight individual fractional data sets. Data for both R217E structures are from a single crystal. ^cLigand includes detergent and solvent molecules. ^dTight geometry constraints were imposed at a later stage of refinement to improve the model quality.

R1–R4 charges appear to fit through an in-plane semicircular arrangement of hydrophobic side chains formed by residues I126, F161 and I190 (Fig. 2a). This feature is the obvious equivalent of the so-called hydrophobic plug²⁹ or charge-transfer center³⁰ in K⁺ channels, functioning as an effective dielectric barrier to the permeation of water and ions and defining the extra- and intracellular sides of the transmembrane electric field (Fig. 2b). R3 is in the unique position of being in plane with the hydrophobic gasket, presumably at the center of the

focused electric field, whereas both R1 and R2 are located well above, and R4 is below the gasket.

A structural comparison of the up conformation of Ci-VSD with all existing voltage-sensor structures provides key insights in relation to the general organization of the gating charges and countercharges. We performed backbone alignments of the S1, S2 and S3a helices from the currently available voltage sensor structures; these include VSDs from two distinct archetypes of K⁺ channels (KvAP and Kv1.2 chimera) and two prokaryotic Na⁺ channels (NavAb and NavRh) (Fig. 2e). Beyond the decent agreement on the VSD scaffold, three main observations can be derived from this comparison. First, although all structures represent (in principle) the activated conformation of each sensor, there is a remarkable difference in the positions of the gating charges. Second, gating charges appear to follow a neat arched path, in which KvAP represents the topmost range of positions and Ci-VSD the bottom. Indeed, the distance between the R1 backbone of KvAP and Ci-VSD at activated states is ~21 Å, which is larger than the proposed conformation change for any VSD. Third, positional heterogeneity also extends to the number and placement of the putative countercharges that serve as electro-

static partners to the individual gating charges (Fig. 2e). These countercharges are located throughout S1, S2 and/or S3 among different sensors, according to their propensity to establish stable ion pairings with selected gating charges. Because the heterogeneity between VSD

Figure 2 Structure of Ci-VSD R217E in the activated (up) conformation.

(a) Side view (left; with extracellular side at top) and top view (right; from extracellular side) of the up conformation of Ci-VSD R217E in cartoon representation with S4 colored red. The four positive charges (R223, R226, R229 and R232) are depicted as sticks and colored in a series of blue shades. A well-defined hydrophobic gasket formed by I126, F161 and I190 with a gating charge R229 (R3) is shown. (b) Architecture of the internal and external vestibules, as calculated with HOLE⁵⁶. The narrowest region is surrounded by the hydrophobic gasket at R3 (in yellow). (c) Structure showing all four gating charges forming a neat line perpendicular to the hydrophobic gasket. The negative countercharges (D129, D1; D186, D2 and E183, E3) in S1 and S3 are shown. (d) Structure showing stabilization of the top two arginines, R223 (R1) and R226 (R2) above the hydrophobic gasket, by hydrogen bonds with crystallographic waters (W) between the negative charges D129 and D151. (e) Left, heterogeneity of arginine positions within S4, highlighted with VSD alignment in reference to the Kv1.2 chimera (Kv1.2 ch, emerald). KvAP (yellow, r.m.s. deviation = 1.4 Å), NavRh (orange, r.m.s. deviation = 3.0 Å), NavAb (green, r.m.s. deviation = 1.1 Å) and Ci-VSD R217E (red, r.m.s. deviation = 1.1 Å). R.m.s. deviation is calculated with Cα of aligned region (S1, S2 and S3a) and indicates the general agreement of VSD scaffold. Right, heterogeneity of putative countercharge positions within the VSD scaffold. Only countercharges potentially involved in direct ion pairing with gating charges, on the basis of the crystal structures, are shown.

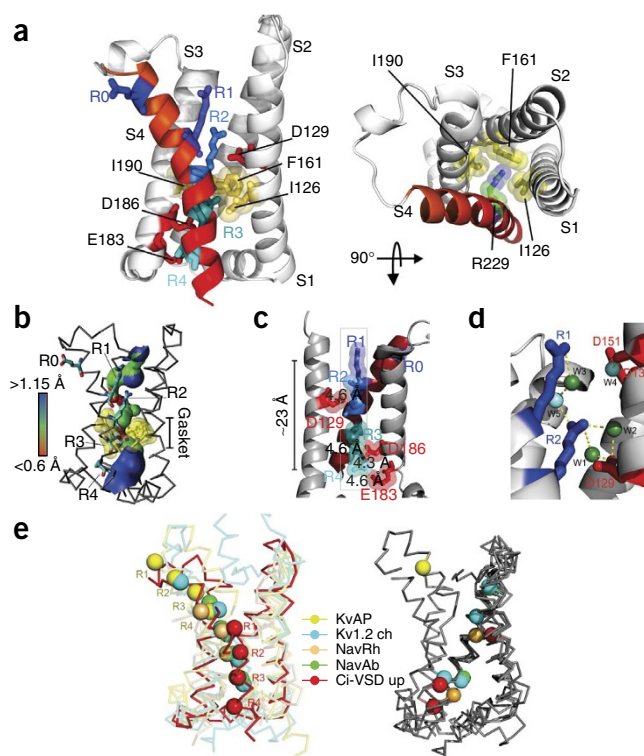


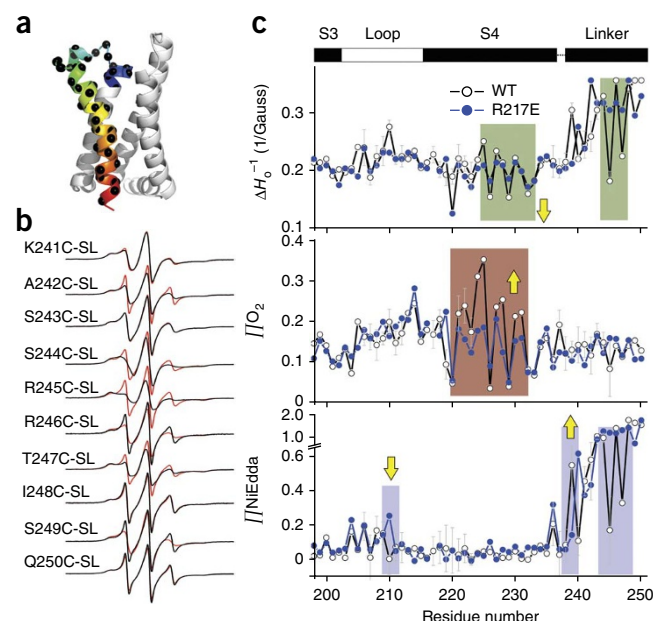
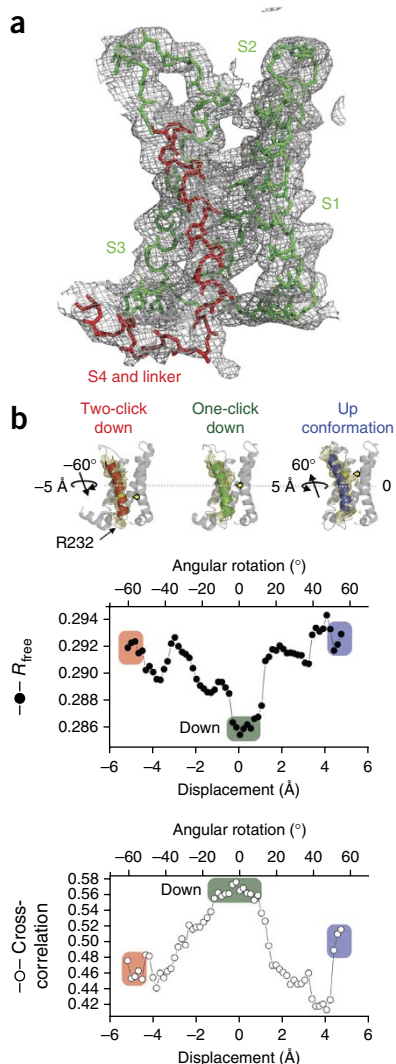
Figure 3 The nature of S4 rearrangement in a lipid environment.

(a) The Ci-VSD R217E structure is shown in ribbon representation with the region studied by site-directed spin-labeling EPR spectroscopy covering the S3-S4 loop and entire S4 and the S4-phosphatase linker colored in rainbow. Black dots indicate the residues modified by spin label. (b) Representative EPR spectra ($n = 3$) for the repeated residues of the S4-phosphatase linker (residues 241–250) on both Ci-VSD WT (black) and R217E (red) background. SL, spin label. (c) Mobility (top), oxygen accessibility (middle) and NiEdda accessibility (bottom) of WT (black) and R217E (blue). Regions with the most interesting changes are highlighted by shaded areas and arrows indicating the direction of the changes: relative to the conformation of R217E, Ci-VSD WT has lower mobility in S4 region and S4-phosphatase linker (green), higher oxygen accessibility in the S4 transmembrane region (brown) and a simultaneous decrease in NiEdda accessibility at the top but an increase at the bottom of S4 (blue). Error bars, s.d. of three independently measured power-saturation experiments.

systems could be larger than the extent of individual conformation changes associated with voltage gating, the present alignment suggests that caution must be taken in the direct comparison of structural information across VSD systems.

Conformational changes in a membrane environment

There is extensive evidence that the lipidic environment has a critical role in the conformation, stability and functional behavior of VSDs^{31–33}.



To examine whether the crystal structures are a reflection of voltage-driven events in a biological membrane, we evaluated the conformation of the S3-S4 hairpin through site-directed spin-labeling EPR spectroscopy of membrane-reconstituted wild-type (WT) Ci-VSD and R217E. For this data set, we made all measurements in the absence of a membrane potential, so the spin-labeled sensors are expected to populate the up state in R217E and the down state for WT Ci-VSD.

We purified 41 cysteine mutants covering the S3-S4 loop, S4 and S4-phosphatase linker (Fig. 3a) in both the WT and R217E background, then spin-labeled and reconstituted them in liposomes (1-hexadecanoyl-2-(9Z-octadecenoyl)-sn-glycero-3-phosphocholine (POPC) and 1-hexadecanoyl-2-(9Z-octadecenoyl)-sn-glycero-3-phospho-(1'-rac-glycerol) (sodium salt) (POPG) in a 3:1 molar ratio²⁶). We focused on two types of dynamic EPR structural information: the spin-probe motional freedom, estimated from the inverse of the central line width of the first-derivative absorption spectra (ΔH_0^{-1}), and the spin-probe solvent accessibility, evaluated by collisional relaxation methods (Fig. 3). Here, nonpolar oxygen (I/O_2) serves as a contrast agent to evaluate membrane exposure, whereas polar Ni(II) ethylenediaminediacetic acid ($I/NiEdda$) reports on the extent of aqueous exposure. The periodicity of I/O_2 oscillations indicates the secondary structure of S4 as an α -helix, and low $I/NiEdda$ levels clearly define the boundaries of S4, both of which agree very well with the Ci-VSD R217E structure. These results suggest that the obtained Ci-VSD R217E crystal structure samples its native conformation in a biological membrane.

Figure 4 Structure of WT Ci-VSD in the resting (down) conformation.

(a) Electron density map ($2F_o - F_c$ at 1.0 σ) of WT Ci-VSD at 3.6-Å resolution. The backbone of S4 and interdomain linker are colored red. (b) Top, three potential models within the electron density map of Ci-VSD WT: two-click down (S4 in red), one-click down (S4 in green) and up conformation (S4 in blue). The first arginines (R232) of the three models are shown with yellow spheres and arrows to illustrate the vertical displacement on the S4 helix. Bottom, measurements of rotation angle and vertical displacement of S4 in reference to the one-click down model. The independent R_{free} values and correlation coefficients were averaged among frames of every 2° rotation for simplicity. The regions corresponding to three models are highlighted by red (two-click down), green (one-click down) and blue (up conformation) backgrounds.

As a first approximation, the spectral data set of Ci-VSD WT (Supplementary Fig. 2) confirms that it is similarly dynamic as the R217E mutant (Fig. 3b), with the exception of gating charges R2, R3 and R4, which become further restricted in motion. This is accompanied by an increase in lipid exposure in the center of S4 (Fig. 3c). Most importantly, aqueous accessibilities (*ITNiEdda*) show simultaneous reduction at the extracellular end of S4 (residue 210) together with an increase at its intracellular end (residue 239) (Fig. 3c). This *ITNiEdda* boundary shift explicitly demonstrates the downward S4 helix movement between up (R217E) and down (WT) conformations. In addition, these accessibility changes suggest a modest vertical displacement (about one residue corresponding to ~ 2 Å).

Larger spectroscopic changes can be seen at the interdomain linker (after residue 236, not present in the R217E crystal structure). In particular, the lower *ITNiEdda* accessibility and lower mobility show that residues 245 and 247 in the S4-phosphatase linker of Ci-VSD WT are probably involved in additional tertiary contacts (Fig. 3c). The nature and extent of these changes are a clear demonstration of propagation of the S4 helix movement into the linker region.

Structure of Ci-VSD at rest

Although we followed a similar strategy to determine the structure of Ci-VSD WT in its down conformation, the crystallization proved to be a keen challenge (Online Methods). We ultimately created the working data set for Ci-VSD WT in complex with Fab 39D10_18 by merging eight fractional data sets. We solved the structure by molecular replacement and refined it to a final $R_{\text{work}}/R_{\text{free}}$ of 26.9/30.3, including data to 3.6 Å for the nominal 3.8-Å data (Fig. 4a and Supplementary Fig. 3a,c). In the down-conformation complex, the Fab binds to a different epitope formed by the external surface between S2 and S3.

We built the Ci-VSD WT structure at backbone level within the continuous electron density map (Fig. 4a), assisted by the R217E structure. Initial analysis of the Ci-VSD WT structure revealed a similar scaffold as that of R217E mutant but with substantial changes associated with the conformation of the S3-S4 loop (Supplementary Fig. 4a) and the addition of distinct electron density toward the

intracellular face of the bundle (Fig. 4a and Supplementary Fig. 4a). We interpreted the additional density as a short (2.5-turn) helix³⁴ corresponding to the interdomain linker that connects the VSD to the phosphatase. At the present resolution, however, crystallographic uncertainty associated with S4 registry needs to be addressed to fully interpret the substantial deviations from the R217E structure. Our repeated attempts to generate and identify electron density markers along S4 were unsuccessful, owing to large and systematic reductions in the quality and resolution of the Ci-VSD WT crystals (Online Methods). Therefore, we developed alternative lines of evidence in support of the present interpretation of the Ci-VSD WT electron density map.

First, EPR data demonstrated that gating charges R2, R3 and R4 in WT are shielded from membrane exposure (low O_2 accessibility) by strong tertiary contacts (low ΔH_o^{-1}). This limits the position of the S4 helix to only three possibilities inside the WT electron density map (Fig. 4b): an up conformation (same S4 position as in the R217E structure), a three-residue downward movement of S4 (one 'click' down) or a six-residue downward movement of S4 (two clicks down).

Second, taking into account that in the Ci-VSD WT data the additional electron density from the S4-phosphatase linker includes all residues in the expressed Ci-VSD construct (up position 244) and reaches the reported N-terminal end of the phosphatase domain³⁵, it represents a useful anchor not only for determining the registry of the S4 helix but also for modeling full-length Ci-VSP in future efforts. In the reference to the one-click down model, the hypothetical up-conformation model shifts the S4 helix three residues upward and leaves unaccounted electron density after the last residue (244) around the S4-phosphatase linker (Supplementary Fig. 4c–e). Fitting the two-click down model shortens the S3-S4 loop, which obviously deviates from the continuous electron density map of the loop (Supplementary Fig. 4b), and positions residue R232 in a water-exposed environment (Fig. 4b). The two-click down model is thus inconsistent with the strong tertiary contact derived from EPR spectroscopy.

Third, we addressed the crystallographic uncertainties directly by an independent computational method, molecular dynamic flexible fitting (xMDFF) for crystallography^{36,37} (Supplementary Fig. 5) to quantitatively evaluate explicit S4 positions within current experimental electron density maps. In addition, we generated potential structural models by gradual shift and rotation of the S4 helix from the up-conformation model to the two-click down model (in all, an ~ 10 -Å vertical displacement and $\sim 110^\circ$ rotation). We independently refined each structural model and calculated two parameters for model evaluation: crystallographic R_{free} value and correlation coefficient (CC) between the experimental density map of the S4

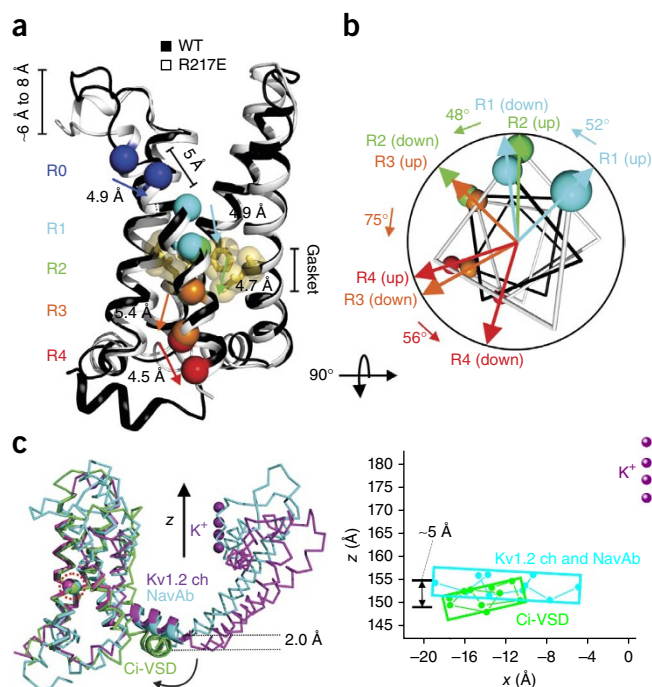
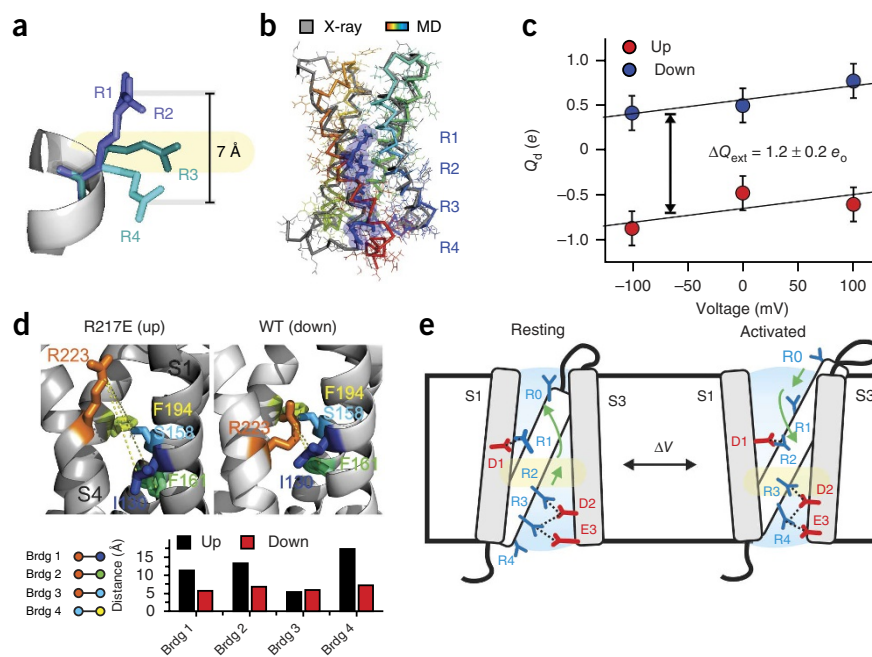


Figure 5 Structural change between Ci-VSD WT and R217E. (a) Overlap of Ci-VSD R217E (white) and WT (black) backbones, showing the conformational changes S3-S4 linker, relative position change in S4 and the existence of the interdomain linker in WT. The axial translations of Cα of the arginines are ~ 5 Å. The four arginines rotate ~ 48 – 75° relative to the helical axis. (b) Helical projection of gating-charge Cα of the WT and R217E structures. (c) Left, structures of Ci-VSD WT (green), Kv1.2 ch (purple) and NavAb (cyan), as superposed through their respective VSDs. Scaffold is shown in ribbon and the conserved phenylalanine as spheres highlighted by the red dotted circle. Right, on the basis of this structural superposition, the S4-phosphate linker of Ci-VSD WT (green) and the S4-S5 linkers from Kv1.2 ch and NavAb (cyan) were projected onto a coordinate framework anchored by the position of the potassium ions in Kv1.2 ch. Helices are shown in rectangular boxes on top of the connected Cα of each residue.

Figure 6 A molecular mechanism of charge translocation in a voltage sensor. **(a)** Comparison of the rotamer distribution of gating arginines in the up conformation resolved in the 2.5-Å crystal structure. **(b)** 105-ns all-atom MD simulation (spectrum) showing stability of the Ci-VSD WT crystal structure (gray). **(c)** Calculation of the displacement charge between the up and down conformations of Ci-VSD at +100, 0 and -100 mV, yielding a gating charge of $1.2 \pm 0.2 e_0$ (averaged among individual frames of last 15-ns simulation). Shown are mean equivalent electronic charges and s.d. **(d)** Top, structures highlighting four existing metal bridge (brdg) constraints for the down state in Shaker: bridge 1, bridge 2 (ref. 29), bridge 3 (ref. 46) and bridge 4 (ref. 30). Bottom, graph showing compatibility only in the down state of Ci-VSD for the three state-dependent bridges (1, 2 and 4). **(e)** Mechanistic model of voltage sensing in Ci-VSD. An ~5-Å downward movement of S4 is accompanied by a counterclockwise ~60° rotation of the entire helix. Arginines in S4 are stabilized by successive negative countercharges on S1 and S3. A potential rotameric reorientation of the arginines might additionally contribute to the overall gating-charge transfer.



region and the calculated electron density from the refined model. The global R_{free} minimum and CC maximum coincide in a region that unambiguously determines the most probable position of the S4 helix (Fig. 4b). The resulting S4 position is three residues lower than that in the R217E structure, and R2, R3 and R4 are placed in a protein environment (away from lipids). This result is in excellent agreement with the one-click down model.

We argue that the one-click down model is the only compatible S4 arrangement to fit both the S3-S4 loop and S4-phosphatase linker in the electron density map, and it is supported by the xMDF data. The model is also in agreement with the direction and modest extent of S4 displacement indicated by the shift in water accessibility (JINiEdda).

DISCUSSION

Molecular basis of gating-charge transfer in VSDs

The structure of Ci-VSD in its down state offers an opportunity to find long-sought answers to questions regarding the mechanism by which voltage influences the conformation of S4. This relative displacement of the S4 helix becomes apparent in alignment of the WT and R217E structures (Fig. 5a): the displacement from the up to the down conformation is ~5 Å downward in every gating charge (including R0). There are no apparent changes in S4 α -helical secondary structure, and there is minimal angular reorientation in relation to S1-S3 during this conformation change. A helical projection of each gating-charge C α of the WT and R217E structures reveals that this downward movement is accompanied by a counterclockwise rotation that varied between 48° and 75°, viewed from the extracellular side (Fig. 5b). During deactivation, the movement of S4 is enabled by a simultaneous reorientation in the S3-S4 loop (Supplementary Fig. 4a). This involves the limited unwinding of a short helical turn (residues 207–210) together with a sharp upward reorientation (6–8 Å) of most of the loop residues.

The nature of the S4 movement described above places the C α of each individual up-conformation arginine essentially in the same position as the following arginine of the down conformation (three residues away, sequence-wise). This way, an ~5-Å one-click charge

displacement (Fig. 5a) is achieved in relation to the hydrophobic gasket. In this gating click, S4 charges transition from a position with electrostatic partners R1-D1, R2-D2 and R3-E3 in the down state (with R4 fully solvated by water) to one in which the pairings are R2-D1, R3-D2 and R4-E3 in the up conformation. R1 thus pushes into the external cavity and becomes fully hydrated. Neither the hydrophobic gasket nor the countercharges in S1 and S3 display sizable changes during S4 movement.

The S3 segment itself does not appear to move substantially nor does its overall conformation appear to be affected by the movements in S4. From a mechanistic standpoint, the present structures and associated conformational rearrangements provide no evidence for a 'paddle'-like correlated movement of the S3-S4 hairpin^{38,39}. In fact, the movements described above are a straightforward representation of the classic 'helix-screw' or 'sliding-helix' concepts independently proposed^{40,41} more than 25 years ago.

The presence of the interdomain linker at the intracellular base of the down conformation of Ci-VSD can serve as a reference point to evaluate the process by which S4 movement triggers downstream rearrangements in the phosphatase domain. Yet, in spite of its higher resolution and the same interaction in crystal lattice, the up-conformation Ci-VSD structure offers no clues as to the structure and overall conformation of the linker (residues 237–244). Nevertheless, we could partially address this question by comparing the Ci-VSD linker conformation with those found on full-length ion channels. Ci-VSD in the down conformation superposed on VSDs from Kv1.2 and NavAb in their up conformation, with an r.m.s. deviation of 1.1 Å on the backbones of S1, S2 and S3a helices (Fig. 5c). Although the orientation of the S4-S5 linker relative to the aligned sensors is the same for NavAb and Kv1.2, the Ci-VSD WT linker swung some 30° (clockwise) and shows an average ~2-Å downward displacement relative to the S4-S5 linker. It is interesting that the vertical difference at the end of S4 between the activated sensors (NavAb and Kv1.2) and the resting sensor (Ci-VSD WT) is ~5 Å (Fig. 5c). This difference coincides with the extent of conformation change between the up and down state of Ci-VSD (Fig. 5a). We suggest that this downward reorientation could represent a physiologically relevant linker

movement and provide a useful window into the putative structural rearrangements that take place during electromechanical coupling.

Electrostatic consequences of S4 movement

Beyond the backbone motion, side chain orientation also indicates interesting details regarding the mechanism of voltage sensing. Superposition of all gating-charge residues from the 2.5-Å R217E crystal structure at the backbone level reveals a remarkable rotameric behavior: along the S4 helix, from R1 to R4, arginine side chains undergo a downwards reorientation (up to ~7 Å) as they first interact and then cross the hydrophobic gasket (Fig. 6a). A survey of the existing high-resolution VSD structures suggests that this appears to be a common characteristic of sensor arginines (Supplementary Fig. 6). Hence, we propose that this rotameric reorientation mechanism could be an additional contributor to the total gating-charge translocation in VSDs.

To better evaluate the structural rearrangements informed by the down and up Ci-VSD conformations, we modeled the full complement of side chains in the down structure to generate all-atom models for both Ci-VSD WT and R217E, both of which are stable after an ~105-ns molecular dynamics (MD) simulation in explicit membrane and solvent (Fig. 6b). We set out to determine, on the basis of the all-atom models, the amount of charge transferred by the one-click gating rearrangement from the average displacement charge difference ΔQ_d between two conformations (the Q-route formalism⁴²). We calculated the time-averaged displacement charge during 20 ns of simulation at each of three transmembrane potentials (−100, 0 and +100 mV) (Fig. 6c). From these calculations, we estimated the magnitude of the calculated gating charge at $1.2 \pm 0.2 e_0$, remarkably close to the expected value from gating-current measurements ($\sim 1 e_0$)^{17,22}. The present calculation is an indication that the one-click charge translocation is able to account for the transfer of at least one electronic gating charge, results in agreement with the characteristic shallow voltage dependence of Ci-VSD (Fig. 1b)¹⁷.

Implications for the general gating mechanism in other VSDs

It seems to be generally agreed that, in spite of long evolutionary distances and the obvious differences in structure and functional set points, voltage sensing in VSDs is based on a common structural blueprint. The determination of the crystal structures of Ci-VSD in the up and down conformations reveals an explicit mechanism of voltage activation that recapitulates the basic tenets of the helical-screw or sliding-helix models^{40,41} in voltage-sensing phosphatases. But is this mechanism an effective model to understand ion channel-based electrical excitability?

A quick survey of the voltage dependence of ion channels, proton channels and voltage-dependent enzymes illustrates the large heterogeneity that exists in regards to the estimated charge transferred (z_0 from ~1 to ~3.6 e_0 per VSD) and the amount of energy required to activate the system ($V_{1/2}$ from −120 to +80 mV). We point out that the key mechanistic differences in regards to voltage sensing are likely to be derived from heterogeneity in gating-charge positions in the VSD scaffold and their interactions with the coevolved countercharges. These interactions define not only the overall transferred charge required for function but also the extent of S4 movement needed to fulfill a given charge translocation.

Several lines of evidence suggest that relatively modest S4 movements such as those observed in Ci-VSD conform to the extensive experimental data that exist for voltage-gated channels. Most of the available cysteine reactivity data (surveyed in ref. 43) can be readily accommodated with S4 movements in the vicinity of 5 Å. In addition,

distance estimations on Shaker R1 from tethered charges of different length suggest that S4 moves ~4 Å (ref. 44). The present gating model is also compatible with recent luminescence resonance energy transfer and fluorescence data⁴⁵ showing 5-Å to 7-Å S4 vertical displacements in Shaker channels. Explicit distance constraints for the down conformation of the Shaker VSD have recently been obtained from metal-bridging experiments that link S4 with S1 (Cd²⁺ bridge 1 (ref. 29)), S4 with S2 (Cd²⁺ bridge 2 (ref. 29)) and S2 with S3 (Mg²⁺ bridge 3 (ref. 46)). In addition, direct electrostatic interactions have been identified between R1 and F194 in S3 (bridge 4 (ref. 30)). Taking as a reference Ci-VSD residue R223 in S4 as the functional equivalent of Shaker R1, we tested the compatibility of these distance constraints with the up and down Ci-VSD structures (Fig. 6d). When evaluated on the R217E structure, the observed distances exceeded 10 Å, well beyond the range for cysteine-driven Cd²⁺ bridges. But when we carried out the same exercise on the WT (down) structure, all distances were within the experimental range of Cd²⁺ bridges. The compatibility of bridge 3 with both up and down structures is expected, because the relative positions of S2 and S3 do not change during gating.

In order to account for the three or four electronic charges needed to gate Shaker (and other K⁺ channels), we can interpret our structures in two different contexts. On the one hand, it is possible that Ci-VSD undergoes a larger motion than what is reflected in the present crystal structures. In this case WT Ci-VSD would represent an intermediate state on its way to the down conformation. The limited changes in accessibility from EPR experiments of membrane-embedded Ci-VSD tend not to support this option. On the other hand, an alternative possibility is that, despite sharing a similar helical-screw mechanism, the S4 helices in voltage-dependent channels would move further than that in Ci-VSD to accommodate the additional charge transfer. For instance, a two-click gating motion would extend the movement of S4 to ~10 Å and its rotation to 110–180°, an option supported by recent metal ion–bridge experiments⁴⁷. Indeed, a comparison of the WT Ci-VSD structure to that of computationally derived down conformations^{48,49} requires an additional 8-Å to 10-Å displacement to match the gating charges. This suggests a larger sliding-helix movement for voltage-gated channels. However, very recent experiments with chimeras of Ci-VSD and the viral K⁺ channel Kcv beautifully show that voltage-dependent rearrangements of Ci-VSD, putatively a one-click sensor, are sufficient and necessary to gate a K⁺-selective pore⁵⁰.

Our structures are incompatible with data supporting simple ‘field-rearrangement’ models, in which S4 movement is minimal⁵¹. Similarly, fluorescence data predicting ~180° S4 rotations⁵² would require two or three additional gating-translocating clicks to comply with this rotational flip. The overall exposure of S4 to the lipid environment is incompatible with the original description of the S4 ‘gating canal’⁸ or canaliculus⁵³. Finally, observations in support of very large S4 movements from biotin-streptavidin trapping experiments^{38,39} or mass-tagging approaches^{33,54} require separate consideration⁵⁵, given the present lack of evidence for the functional existence of an S3–S4 paddle.

In summary, we suggest that voltage-dependent activation in Ci-VSP is best illustrated through the basic diagram in Figure 6. Upon depolarization, the S4 segment undergoes an ~5-Å outward translation along its main axis in concert with an ~60° clockwise rotation. As a consequence, linearly aligned gating charges R1–R4 undergo a one-click displacement that translocates R2 through a dielectrically tight hydrophobic gasket, while exchanging electrostatic partners with countercharges D1, D2 and E3 in helices S1 and S3. As S4 translocates, the flexible arginine side chains in R2 and R3

putatively undergo a rotameric upward flip that potentially contributes to the charge transfer process. We propose that relatively subtle variations of this general mechanism should help explain voltage-dependent activation in many excitable systems.

METHODS

Methods and any associated references are available in the [online version of the paper](#).

Accession codes. Coordinates and structure factors have been deposited in the Protein Data Bank under accession codes **4G7V** (2.5-Å data for R217E mutant), **4G7Y** (2.8-Å data for R217E mutant) and **4G80** (3.8-Å data for WT).

Note: Any Supplementary Information and Source Data files are available in the [online version of the paper](#).

ACKNOWLEDGMENTS

We are thankful to K. Rajashankar and the staff at the NE-CAT 24-ID beamline as well as to R. Sanishvili and the staff at the GM/CA 23-ID beamline in the Advanced Photon Source, Argonne National Laboratory. We thank the Perozo, Bezanilla and Roux laboratories for illuminating discussions and invaluable experimental advice and A. Koide and S. Koide (University of Chicago) for the antibody library. We are grateful to E.J. Adams, R. Keenan, P. Rice and X. Yang for helpful crystallographic advice. The US National Resource provided Anton computer time for Biomedical Supercomputing and the Pittsburgh Supercomputing Center through grants RC2GM093307 and PSCA13070P (to E.P.) from the US National Institutes of Health. This work was supported in part by US National Institutes of Health grants R01-GM57846 (to E.P.), U54-GM74946 (to E.P.), R01-GM062342 (to B.R.), 9P41-GM104601 (to K.S.), U54-GM087519 (to K.S.) and 5R01-GM098243-02 (to K.S.) and a Beckman Postdoctoral Fellowship to A.S.

AUTHOR CONTRIBUTIONS

E.P. and Q.L. designed experiments. Q.L. and S.W. performed biochemical experiments. M.P., Q.L. and A.K. selected Fab by phage-display methods. Q.L., S.W., R.E.H. and E.P. collected crystallographic data. Q.L. analyzed crystallographic data. D.M. and B.R. performed MD simulations to estimate the gating charge. A.S., R.M. and K.S. developed and applied the xMDF method. C.A.V.-G. and Q.L. performed electrophysiological measurements. E.P. and Q.L. wrote the manuscript.

COMPETING FINANCIAL INTERESTS

The authors declare no competing financial interests.

Reprints and permissions information is available online at <http://www.nature.com/reprints/index.html>.

- Hodgkin, A.L. & Huxley, A.F. A quantitative description of membrane current and its application to conduction and excitation in nerve. *J. Physiol. (Lond.)* **117**, 500–544 (1952).
- Armstrong, C.M. & Bezanilla, F. Currents related to movement of gating particles of sodium channels. *Nature* **242**, 459–461 (1973).
- Bezanilla, F. How membrane proteins sense voltage. *Nat. Rev. Mol. Cell Biol.* **9**, 323–332 (2008).
- Catterall, W.A. Ion channel voltage sensors: structure, function, and pathophysiology. *Neuron* **67**, 915–928 (2010).
- Swartz, K.J. Sensing voltage across lipid membranes. *Nature* **456**, 891–897 (2008).
- Stühmer, W. *et al.* Structural parts involved in activation and inactivation of the sodium channel. *Nature* **339**, 597–603 (1989).
- Papazian, D.M., Timpe, L.C., Jan, Y.N. & Jan, L.Y. Alteration of voltage-dependence of Shaker potassium channel by mutations in the S4 sequence. *Nature* **349**, 305–310 (1991).
- Yang, N., George, A.L. Jr. & Horn, R. Molecular basis of charge movement in voltage-gated sodium channels. *Neuron* **16**, 113–122 (1996).
- Yang, N. & Horn, R. Evidence for voltage-dependent S4 movement in sodium channels. *Neuron* **15**, 213–218 (1995).
- Mannuzzu, L.M., Moronne, M.M. & Isacoff, E.Y. Direct physical measure of conformational rearrangement underlying potassium channel gating. *Science* **271**, 213–216 (1996).
- Cha, A. & Bezanilla, F. Characterizing voltage-dependent conformational changes in the Shaker K⁺ channel with fluorescence. *Neuron* **19**, 1127–1140 (1997).
- Jiang, Y. *et al.* X-ray structure of a voltage-dependent K⁺ channel. *Nature* **423**, 33–41 (2003).
- Long, S.B., Campbell, E.B. & MacKinnon, R. Crystal structure of a mammalian voltage-dependent Shaker family K⁺ channel. *Science* **309**, 897–903 (2005).
- Long, S.B., Tao, X., Campbell, E.B. & MacKinnon, R. Atomic structure of a voltage-dependent K⁺ channel in a lipid membrane-like environment. *Nature* **450**, 376–382 (2007).
- Payandeh, J., Scheuer, T., Zheng, N. & Catterall, W.A. The crystal structure of a voltage-gated sodium channel. *Nature* **475**, 353–358 (2011).
- Zhang, X. *et al.* Crystal structure of an orthologue of the NaChBac voltage-gated sodium channel. *Nature* **486**, 130–134 (2012).
- Murata, Y., Iwasaki, H., Sasaki, M., Inaba, K. & Okamura, Y. Phosphoinositide phosphatase activity coupled to an intrinsic voltage sensor. *Nature* **435**, 1239–1243 (2005).
- Ramsey, I.S., Moran, M.M., Chong, J.A. & Clapham, D.E. A voltage-gated proton-selective channel lacking the pore domain. *Nature* **440**, 1213–1216 (2006).
- Sasaki, M., Takagi, M. & Okamura, Y. A voltage sensor-domain protein is a voltage-gated proton channel. *Science* **312**, 589–592 (2006).
- Matsuda, M. *et al.* Crystal structure of the cytoplasmic phosphatase and tensin homolog (PTEN)-like region of *Ciona intestinalis* voltage-sensing phosphatase provides insight into substrate specificity and redox regulation of the phosphoinositide phosphatase activity. *J. Biol. Chem.* **286**, 23368–23377 (2011).
- Armstrong, C.M. & Bezanilla, F. Currents related to movement of the gating particles of the sodium channels. *Nature* **242**, 459–461 (1973).
- Villalba-Galea, C.A., Sandtner, W., Starace, D.M. & Bezanilla, F. S4-based voltage sensors have three major conformations. *Proc. Natl. Acad. Sci. USA* **105**, 17600–17607 (2008).
- Kohout, S.C., Ulbrich, M.H., Bell, S.C. & Isacoff, E.Y. Subunit organization and functional transitions in Ci-VSP. *Nat. Struct. Mol. Biol.* **15**, 106–108 (2008).
- Dimitrov, D. *et al.* Engineering and characterization of an enhanced fluorescent protein voltage sensor. *PLoS ONE* **2**, e440 (2007).
- Villalba-Galea, C.A., Frezza, L., Sandtner, W. & Bezanilla, F. Sensing charges of the *Ciona intestinalis* voltage-sensing phosphatase. *J. Gen. Physiol.* **142**, 543–555 (2013).
- Li, Q., Jogini, V., Wanderling, S., Cortes, D.M. & Perozo, E. Expression, purification, and reconstitution of the voltage-sensing domain from Ci-VSP. *Biochemistry* **51**, 8132–8142 (2012).
- Fellouse, F.A. *et al.* High-throughput generation of synthetic antibodies from highly functional minimalist phage-displayed libraries. *J. Mol. Biol.* **373**, 924–940 (2007).
- Villalba-Galea, C.A., Frezza, L., Sandtner, W. & Bezanilla, F. Sensing charges of the *Ciona intestinalis* voltage-sensing phosphatase. *J. Gen. Physiol.* **142**, 543–555 (2013).
- Campos, F.V., Chanda, B., Roux, B. & Bezanilla, F. Two atomic constraints unambiguously position the S4 segment relative to S1 and S2 segments in the closed state of Shaker K channel. *Proc. Natl. Acad. Sci. USA* **104**, 7904–7909 (2007).
- Tao, X., Lee, A., Limapichat, W., Dougherty, D.A. & MacKinnon, R. A gating charge transfer center in voltage sensors. *Science* **328**, 67–73 (2010).
- Schmidt, D., Jiang, Q.X. & MacKinnon, R. Phospholipids and the origin of cationic gating charges in voltage sensors. *Nature* **444**, 775–779 (2006).
- Ramu, Y., Xu, Y. & Lu, Z. Enzymatic activation of voltage-gated potassium channels. *Nature* **442**, 696–699 (2006).
- Zheng, H., Liu, W., Anderson, L.Y. & Jiang, Q.X. Lipid-dependent gating of a voltage-gated potassium channel. *Nat. Commun.* **2**, 250 (2011).
- Hack, N.J., Smith, G.P. & Peters, T.J. Subcellular localization and properties of lipase activities in human polymorphonuclear leukocytes. *Biochim. Biophys. Acta* **833**, 406–411 (1985).
- Kohout, S.C. *et al.* Electrochemical coupling in the voltage-dependent phosphatase Ci-VSP. *Nat. Chem. Biol.* **6**, 369–375 (2010).
- Trabuco, L.G., Villa, E., Mitra, K., Frank, J. & Schulten, K. Flexible fitting of atomic structures into electron microscopy maps using molecular dynamics. *Structure* **16**, 673–683 (2008).
- Trabuco, L.G., Villa, E., Schreiner, E., Harrison, C.B. & Schulten, K. Molecular dynamics flexible fitting: a practical guide to combine cryo-electron microscopy and X-ray crystallography. *Methods* **49**, 174–180 (2009).
- Ruta, V., Chen, J. & MacKinnon, R. Calibrated measurement of gating-charge arginine displacement in the KvAP voltage-dependent K⁺ channel. *Cell* **123**, 463–475 (2005).
- Jiang, Y., Ruta, V., Chen, J., Lee, A. & MacKinnon, R. The principle of gating charge movement in a voltage-dependent K⁺ channel. *Nature* **423**, 42–48 (2003).
- Catterall, W.A. Molecular properties of voltage-sensitive sodium channels. *Annu. Rev. Biochem.* **55**, 953–985 (1986).
- Guy, H.R. & Seetharamulu, P. Molecular model of the action potential sodium channel. *Proc. Natl. Acad. Sci. USA* **83**, 508–512 (1986).
- Roux, B. The membrane potential and its representation by a constant electric field in computer simulations. *Biophys. J.* **95**, 4205–4216 (2008).
- Tombola, F., Pathak, M.M. & Isacoff, E.Y. How does voltage open an ion channel? *Annu. Rev. Cell Dev. Biol.* **22**, 23–52 (2006).
- Ahern, C.A. & Horn, R. Focused electric field across the voltage sensor of potassium channels. *Neuron* **48**, 25–29 (2005).
- Posson, D.J. & Selvin, P.R. Extent of voltage sensor movement during gating of shaker K⁺ channels. *Neuron* **59**, 98–109 (2008).

46. Lin, M.C., Abramson, J. & Papazian, D.M. Transfer of ion binding site from ether-a-go-go to Shaker: Mg²⁺ binds to resting state to modulate channel opening. *J. Gen. Physiol.* **135**, 415–431 (2010).
47. Henrion, U. *et al.* Tracking a complete voltage-sensor cycle with metal-ion bridges. *Proc. Natl. Acad. Sci. USA* **109**, 8552–8557 (2012).
48. Vargas, E., Bezanilla, F. & Roux, B. In search of a consensus model of the resting state of a voltage-sensing domain. *Neuron* **72**, 713–720 (2011).
49. Jensen, M.Ø. *et al.* Mechanism of voltage gating in potassium channels. *Science* **336**, 229–233 (2012).
50. Arrigoni, C. *et al.* The voltage-sensing domain of a phosphatase gates the pore of a potassium channel. *J. Gen. Physiol.* **141**, 389–395 (2013).
51. Cha, A., Snyder, G.E., Selvin, P.R. & Bezanilla, F. Atomic scale movement of the voltage-sensing region in a potassium channel measured via spectroscopy. *Nature* **402**, 809–813 (1999).
52. Glauner, K.S., Mannuzzu, L.M., Gandhi, C.S. & Isacoff, E.Y. Spectroscopic mapping of voltage sensor movement in the Shaker potassium channel. *Nature* **402**, 813–817 (1999).
53. Goldstein, S.A. A structural vignette common to voltage sensors and conduction pores: canaliculi. *Neuron* **16**, 717–722 (1996).
54. Koag, M.C. & Papazian, D.M. Voltage-dependent conformational changes of KVAP S4 segment in bacterial membrane environment. *Channels (Austin)* **3**, 356–365 (2009).
55. Li, Q., Wanderling, S., Sompornpisut, P. & Perozo, E. Structural basis of lipid-driven conformational transitions in the KvAP voltage-sensing domain. *Nat. Struct. Mol. Biol.* **21**, 160–166 (2014).
56. Smart, O.S., Neduvellil, J.G., Wang, X., Wallace, B.A. & Sansom, M.S. HOLE: a program for the analysis of the pore dimensions of ion channel structural models. *J. Mol. Graph.* **14**, 354–360, 376 (1996).

ONLINE METHODS

Electrophysiology. WT and mutant constructs of Ci-VSD (R217E and R217Q) were made on a phosphatase-inactive mutant C363S background and expressed in *Xenopus laevis* oocytes. 2–3 d after injection, transient sensing currents were recorded with a cut-open oocyte voltage clamp according to published methods^{2,22}. There was no subtraction of leak components during acquisition. The net charge was calculated by integration of the ‘off’ sensing currents at each potential within the whole 500-ms pulse. Data acquisition and analysis were carried out with in-house programs.

Protein expression and purification. The VSD of Ci-VSD (Ci-VSD) was expressed and purified as described²⁶. DNA for the VSD encoding residues 1–260 was cloned into a pQE32 expression vector (Qiagen). The protein was expressed in *E. coli* XL10-Gold. Cells were grown at 37 °C and induced with 0.65 mM IPTG for 3 h at 30 °C (OD₆₀₀ of 0.5–0.7). The protein was purified by two sequential steps by metal-affinity chromatography with cobalt resin (Clontech) and size-exclusion chromatography with a Superdex 200 HR 10/30 column (GE Healthcare). Various truncations and tagged constructs were generated for crystallization purposes. The constructs for the reported crystal structures correspond to residues 106–244 for WT and 89–260 for the R217E mutant. Expression and purification protocols for the truncations are the same as for Ci-VSD_{1–260}.

For selenomethionine incorporation of Ci-VSD WT_{106–244}, cells were pelleted down around OD₆₀₀ = 0.8 before induction. After being rinsed with DI water, pellets from a 3-l culture (in LB) were transferred into 1 l of M9 minimum medium supplemented with 100 µg/mL ampicillin, 0.4% glucose, 2 mM MgSO₄, 0.1 mM CaCl₂, 1× MEM vitamin mix (Invitrogen), 100 mg lysine, 100 mg phenylalanine, 100 mg threonine, 50 mg isoleucine, 50 mg leucine, 50 mg valine and 60 mg selenomethionine. Protein expression was induced with 0.65 mM IPTG for 6 h at 30 °C, and proteins were purified with methods described above.

Antibody screening, expression and purification. WT and R217E mutant of Ci-VSD_{1–260} constructs were biotinylated through amine coupling with NHS-SS-PEG4-biotin (Thermo Scientific). Phage-display selections were performed with a synthetic antibody library built on the 4D5 Fab scaffold as described previously²⁷. Target protein concentrations were serially adjusted with 100 nM in the first round and 10 nM and 5 nM in subsequent rounds to ensure proper stringency. The conformation-specific binders were selected with a competitive selection strategy in which 1 µM nonbiotinylated competitor (such as Ci-VSD WT) was added to the phage library before the incubation with the actual selection target (such as Ci-VSD R217E). All steps were performed in appropriate detergents (1 mM Anzergent 3-14, 2 mM LDAO or 4 mM DM) including a single-point competitive ELISA step used to identify positive clones. Initial hits were also characterized by surface plasmon resonance (SPR) to establish binding affinities. Fabs were expressed in *E. coli* strain 55244 in phosphate-depleted media as described previously⁵⁷. The cells were lysed with a microfluidizer (Avestin Inc.) in PBS buffer and heat-treated at 65 °C for 0.5 h to remove bulk amounts of contaminants. Fabs were then purified with an automated two-step protocol using a custom-built AKTA purification system with 5-ml Protein A Sepharose 4 Fast Flow and 1-ml Resource S (GE Healthcare) columns. Fractions were verified by SDS-PAGE, pooled and dialyzed against PBS. In total, 40 positive clones from four selections were expressed in large scale, complexed with Ci-VSD and tested by size-exclusion chromatography with a Superdex 200 HR 10/30 column (GE Healthcare) against a set of detergents (OG, NG, DM, LDAO, UDM, FosC-12, Cymal-6, UDM, Mega-9, Mega-10, C8E4, Anzergent 3-12 and Anzergent 3-14). The complexes were ranked by homogeneity and stability to set up crystallization trials.

Protein crystallization. The Ci-VSD R217E_{89–260} with Fab 33F12_4 complex was purified in 20 mM Tris, pH 8.0, 150 mM NaCl and 4 mM LDAO. Crystals were grown by hanging-drop vapor diffusion at 20 °C by mixture of 0.1 µL of protein and 0.1 µL reservoir solutions with the Mosquito robotic system (TTP LabTech). Crystals were grown with 100 µL reservoir solution of 0.1 M SPG, pH 8.0, 20% PEG 1500, 10% glycerol or 0.1 M bicine, pH 9.0, 0.3 M MgCl₂, 24% PEG 2000, and 10% glycerol. Diffracting crystals were of space group *P*₆₃22 with cell dimensions *a* = *b* = 121 Å, and *c* = 230 Å; $\alpha = \beta = 90^\circ$, and $\gamma = 120^\circ$ and contained one Ci-VSD R217E and Fab complex in the asymmetric unit (Supplementary Fig. 1a). Cryoprotection was achieved by increasing glycerol concentration to 5%.

The Ci-VSD WT_{106–244} with Fab 39D10_18 complex was purified in 20 mM Tris, pH 8.0, 150 mM NaCl, 1 mM LDAO and 2 mM DM. Crystals were grown by hanging-drop vapor diffusion at 20 °C, with mixture of equal volumes (0.1–2 µL) of protein and reservoir solutions. Crystals were grown with a reservoir solution of 0.1 M Na citrate, pH 5.5, 0.1 M Li₂SO₄, 20% PEG 1000, and 10% glycerol. Crystals were of space group *P*₁ with cell dimensions *a* = 77.3 Å, *b* = 94.2 Å, and *c* = 193.9 Å; $\alpha = 102.6^\circ$, $\beta = 93.5^\circ$, and $\gamma = 105.3^\circ$ and contained four Ci-VSD WT and Fab complexes in the asymmetric unit (Supplementary Fig. 1b). Cryoprotection was achieved by increasing glycerol concentration to 5%.

Data collection. All data were collected at the Advanced Photon Source synchrotron (beamlines 24-ID-E, 24-ID-C, 23-ID-B or 23-ID-D) under a nitrogen stream at 100 K and processed with HKL2000. For the Ci-VSD R217E–33F12_4 complex, a single-rod (needle)-shaped crystal (~20 µm × 30 µm × 100 µm dimension) was used to collect the complete data set by continuous vector-scan collection with a 20-µm microfocused beam. For the Ci-VSD WT–39D10_18 complex, *P*₁ space group crystals contained multiple lattices. Owing to the small size (~10 µm × 40 µm × 50 µm dimension) and weak diffraction of the crystals, data had to be collected without attenuation for at least a 2-s exposure per frame to obtain the highest resolution. Only partial data sets (~20–60% completeness) could be collected from single crystals, owing to severe radiation damage. Overall, 40 fractional data sets of ~3.6–4.5 Å were collected and processed from >1,000 screened crystals. From these, a total of eight fractional data sets were compatibly merged into a nominal 3.8-Å data set. The unit-cell dimensions and angles for the merged data set were adjusted to the average values from the eight individual sets with ~1.5-Å deviation on dimensions and ~1° on angles.

Structure determination. The final Ci-VSD R217E structures were refined to $R_{\text{work}}/R_{\text{free}} = 0.173/0.236$ (for 2.5-Å data set with Ramachandran statistics of 97.0% favored, 2.5% allowed and 0% outlier) and $R_{\text{work}}/R_{\text{free}} = 0.173/0.261$ (for 2.8-Å data set with Ramachandran statistics of 92.1% favored, 7.3% allowed and 0.5% outlier) containing residues 101–236 for Ci-VSD R217E. The side chains are well resolved throughout the Ci-VSD R217E–33F12_4 complex including the voltage sensor as shown by the 2F_o – F_c electron density map at 2.5-Å resolution (Supplementary Fig. 1b,c).

Phases for the Ci-VSD WT–39D10_18 data were determined by molecular replacement with the Fab and Ci-VSD R217E as search models. As the electron density improved after iterative adjustment and refinement, differences between the Ci-VSD WT electron density map and the search model became evident. Starting from residues 200 in the S3-S4 loop (Supplementary Fig. 4a), these discrepancies could not be matched by simple backbone adjustment, and as a consequence, all residues from the loop to the end of the protein were trimmed and rebuilt. Several obvious electron density ‘knobs’ helped position a series of adjacent bulky residues (F199, Y200, E205 and R223; Supplementary Fig. 4a). Aided by density modification and B-factor sharpening⁵⁸, the WT model was built to residue 244, the last amino acid of the construct used for crystallization. This density extends considerably beyond the last visible residue in the Ci-VSD R217E structure (residue 236), which is part of a short helix that represents the linker between the VSD and the phosphatase domains. Four-fold NCS with strict backbone and moderate side chain was imposed separately on the three individual domains: Ci-VSD WT, the variable domain of Fab and the constant domain of Fab. The WT model was refined to $R_{\text{work}}/R_{\text{free}} = 0.248/0.292$, including data to 3.6-Å resolution ($I/\sigma I = 1.0$ with 83% completeness at highest shell). Stringent geometric constraints on bond length and angle were imposed at the last stage of refinement to improve the quality of the structural model. The Ramachandran statistics of the final model are 93.8% favored, 5.7% allowed and 0.5% outlier.

In the down-conformation sensor structure, there are four Ci-VSD WT–39D10_18 complexes in the asymmetric unit of the *P*₁ space group. The major differences among the four copies result from the flexibility between the individual domains (up to 12-Å deviation at the constant domain of the Fab when aligned at Ci-VSD WT; Supplementary Fig. 3d). The constant and variable domains of the Fab are essentially identical (Supplementary Fig. 3d). The four copies of the Ci-VSD WT are also identical, except at the interdomain S4-phosphatase linker, which is present in only three out of four copies (Supplementary Fig. 3e). This heterogeneity suggests an intrinsic structural diversity of the linker region, because the S4 helices in all four Ci-VSD WT copies experience the same dimer-interface interactions in the crystal lattice.

In contrast, no linker is visible at even higher resolution (2.5 Å) in the Ci-VSD R217E structure. This comparison points to the intrinsic dynamics of the interdomain linker; that is, the linker is relatively more stable in the down state in Ci-VSD WT than in the up state in Ci-VSD R217E.

Additional electron-marker strategies in the Ci-VSD WT complex. In an attempt to improve the diffracting properties of the Ci-VSD WT crystals, we carried out a sustained and extensive exploration of additional conditions, including different antibodies, various truncations of the Ci-VSD, further detergent addition and additive screening. These attempts proved unsuccessful in improving the resolution of the Ci-VSD WT data past 3.6 Å. Subsequently, we focused our efforts to place an electron density marker on the S4 of Ci-VSD WT as a way to additionally confirm the S4 helix position. The approaches were carried out through either mercuric compound labeling on engineered cysteine residues or SeMet incorporation through engineered methionines.

For mercury modification, two extra single cysteines were introduced at positions 218 and 228 on Ci-VSD WT_{106–244}. These single-cysteine Ci-VSD mutants generated similar crystals as did native WT. Four mercury-containing compounds (mercury(II) chloride, methyl mercury chloride, ethyl mercury chloride and *p*-chloromercuribenzoic acid) were added to Ci-VSD cysteine mutant at various stages of the crystallization process: before complex with antibody; during cocrystallization or soaking; or after crystallization by application of labeling powder directly onto the crystal drop. 5-min soaking with 1 mM mercury(II) chloride severely compromised diffraction properties without any noticeable changes in crystal size or shape. We were able to obtain several data sets (4.1–4.5 Å) by cocrystallization with up to 2 mM methyl mercury and ethyl mercury. However, we found no mercury signal on either difference or anomalous maps. Cocrystallization at higher mercury concentrations (>5 mM) failed to produce crystals. Ci-VSD single-cysteine mutants were also modified by mercury-containing compounds and purified before formation of the antibody complex. The resulting crystals were much smaller than native crystals and never diffracted better than 5 Å. We were able to collect a 6.5-Å data at 85% completeness from a single crystal. Even though the X-ray fluorescence confirmed the existence of mercury in the crystal, no mercury signal was present in either the difference or anomalous map. These data point to an intrinsic inability to generate Ci-VSD WT diffracting crystals in the presence of a wide range of mercury modifications.

As an alternative, two additional single methionines were introduced at positions 218 and 228 on Ci-VSD WT_{106–244} for SeMet incorporation. The crystals from methionine mutants with 39D10_18 Fab were smaller and softer than native WT crystals and were stable for only ~4–5 d before gradually fading away. Nevertheless, X-ray fluorescence and edge scanning confirmed successful selenium incorporation in the crystals. Inconveniently, they diffracted far worse than did the native crystals. After screening ~300 SeMet crystals, we managed to collect, at best, a 7-Å data set from Ci-VSD 218M–39D10_18 complex with 80% completeness, and its anomalous map contained only one confident methionine M133 on the S chain among 28 potential sites within four copies of the complex in the whole ASU. We attempted to improve the anomalous data by merging different data sets with improved statistics (including completeness, resolution, and $I/\sigma I$) and satisfactory R_{merge} , but the resulting electron density map ($2F_o - F_c$) was always worse than the starting partial data. Direct comparison of asymmetric units of four partial low-resolution (~6.5-Å to 7.5-Å) data sets revealed considerable crystal heterogeneity. Within ~2% variation on cell dimensions and angles of the P1 space group, the protein backbone could deviate up to 7 Å among the different models, a fact that explains our inability to merge low-resolution data. Because the SeMet-incorporated crystals diffracted to only ~5–6 Å, and the heterogeneity of the crystals at low resolution prohibited data merging, and the only possibility of success relied on the use of single SeMet crystals to collect complete data, a condition that was not achieved even with standard WT crystals.

Given our unsuccessful attempts to carry out an electron-marker strategy with both mercuric-compound modification and SeMet incorporation, it is reasonable to believe that we have explored the limits of crystallization of the Ci-VSD WT–39D10_18 complex by different methods. This suggests that the quest for higher-resolution Ci-VSD WT data will probably require a restart of our entire crystallization approach.

S4 position in low-resolution crystallographic data by MD flexible fitting. We used a new computational approach, termed xMDFF, for reconstructing all-atom

structures from low-resolution X-ray diffraction data. xMDFF is derived from the highly successful molecular-dynamics flexible fitting (MDFF) methodology, which solves atomic models of biomolecules imaged by cryo-EM. In the MDFF method, an initial atomic model is subjected to a molecular-dynamics simulation with a modified potential-energy function that includes a term derived from the cryo-EM density map^{36,37}. Through this term, atoms experience steering forces, f^{fit} , that locally drive them toward high-density regions, thereby fitting the atoms to the map. For use with low-resolution X-ray crystallography, the MDFF protocol is modified to work with densities derived from molecular replacement, which uses the phases ϕ from a tentative model and the amplitudes $|F|$ from the X-ray diffraction data (Supplementary Fig. 5a,b). The densities are $2mF_o - DF_c$ maps created with the Phenix suite⁵⁹. Next, the tentative model is flexibly fitted into the electron density map with MDFF. In addition to the steering forces derived from the density data, structural restraints are applied to preserve secondary structure of proteins and nucleic acids^{36,37} as well as to ensure stereochemical correctness⁶⁰, thus avoiding overfitting of the model into the map. With phases from the fitted structure and experimental diffraction amplitudes, the electron density is regenerated. The MDFF-fitted structure is then used as an updated model to be fitted to the new map. This way, given the X-ray diffraction amplitude, calculations for updating the electron density map and generating the atomic model will iteratively refine the unknown phase angles. Phase improvement is indicated by a decrease in R factors with subsequent iterations. These iterations continue until the $R_{\text{free}}/R_{\text{work}}$ reaches a minimum or becomes lower than a predefined tolerance. The xMDFF methodology has been tested for six low-resolution (4-Å to 4.5-Å) protein structures of varying sizes (Supplementary Fig. 5c). An improvement in the R_{free} and R_{work} over and above those reported experimentally is observed in almost all the cases. Furthermore, consistently low MolProbity⁶¹ scores and close R_{free} and R_{work} values suggest minimal overfitting in the predicted all-atom geometries. Next, xMDFF was applied to solve the structure of Ci-VSD with 3.6-Å and 4-Å data. Refinement started from a medium-confidence homology model developed with information from 13 proteins. During refinement, the tentative model underwent a remarkable large-scale deformation with an r.m.s. deviation of 5 Å. Unlike many traditional refinement techniques, xMDFF is able to handle these large-scale structural deformations between the initial and final structures. It produced a final R_{free} of 0.27, starting from the initial 0.46. Positioning of the S4 helices is in excellent agreement with the WT structure independently predicted from experiments, with an r.m.s. deviation ranging from 0.4 to 1 Å.

EPR spectroscopy. Details of purification, reconstitution and EPR spectroscopy analyses of single Ci-VSD cysteine mutants has been described previously³. Here, 41 Ci-VSD_{1–260} single-cysteine mutants comprising residues 200–250 on both WT and R217E backgrounds were purified, spin-labeled with (1-oxyl-2,2,5,5-tetramethylpyrrolidin-3-yl) methyl methanethiosulfonate and reconstituted into POPC/POPG 3:1 liposomes. Continuous-wave EPR measurements were done according to a standard protocol^{11–13}. The mobility (ΔH_0^{-1}), NiEDDA accessibility (ITNi) and oxygen accessibility (ΠO_2) were obtained from power-saturation experiments to deduce the dynamic and structural information of membrane-embedded Ci-VSD.

Molecular-dynamic simulations. A total of four all-atom molecular models of the Ci-VSP voltage sensor were built in an explicit POPC membrane environment with CHARMM-GUI⁶²: one of the down state (WT), one of the up state (R217E), and one of each of those two states with only those residues (residues 106–236) resolved in both crystal structures. The two ‘overlap’ structures were precisely identical in atomistic composition. In both up-state systems, the R217E mutation was reversed *in silico*. Proteins were initially placed in the membrane according to established positioning for the up⁶³ and the down states⁴⁸ of the voltage sensor. The CHARMM36 parameter set⁶⁴ was used for lipids, CHARMM22 with CMAP corrections for protein⁶⁵, and the TIP3P⁶⁶ model for waters. The total system size in each case was ~63,000–72,000 atoms including 150 mM KCl. Each of these four systems was run for 20 ns of molecular dynamics at 315 K with the NAMD⁶⁷, with 2-fs time steps, periodic boundary conditions, particle-mesh Ewald electrostatics, and a 12-Å real-space cutoff. The full-length WT structure was run for a total 105 ns, with ANTON⁶⁸, and the full-length up-state model for a total of 60 ns. Additionally, for both of the overlap structures, another 20 ns was performed for applied transmembrane voltages of +100 mV, 0 mV and –100 mV. Also, for the down-state system,

another 95 ns of simulation was performed on ANTON⁶⁸, with the CHARMM27 force field for lipids⁶⁹.

Because the shortened up-state model and the down-state model represent different configurations of an identical atomistic system, they can be used to compute a gating charge⁴². Gating-charge calculations were done with the last 15 ns of each 20-ns simulation, for −100 mV, 0 mV, and +100 mV. For each of the two states of the system, the displacement charge was calculated from trajectories in unwrapped coordinates with the same charge offset⁶³. To look at the interactions between arginine residues on S4 and their countercharges, the NAMD energy plug-in of VMD⁷⁰ was used to compute the electrostatic interaction energies between residues, with the CHARMM force field, for each frame of the molecular-dynamics trajectories: the 95 ns of ANTON trajectory for the down state and the second half of the 10-ns trajectory for the full up state.

57. Rizk, S.S. *et al.* Allosteric control of ligand-binding affinity using engineered conformation-specific effector proteins. *Nat. Struct. Mol. Biol.* **18**, 437–442 (2011).
58. de Vos, A.M. *et al.* Crystal structure of the kringle 2 domain of tissue plasminogen activator at 2.4-Å resolution. *Biochemistry* **31**, 270–279 (1992).
59. Finer-Moore, J.S., Kossiakoff, A.A., Hurley, J.H., Earnest, T. & Stroud, R.M. Solvent structure in crystals of trypsin determined by X-ray and neutron diffraction. *Proteins* **12**, 203–222 (1992).
60. Schreiner, E., Trabuco, L.G., Freddolino, P.L. & Schulten, K. Stereochemical errors and their implications for molecular dynamics simulations. *BMC Bioinformatics* **12**, 190 (2011).
61. Chen, V.B. *et al.* MolProbity: all-atom structure validation for macromolecular crystallography. *Acta Crystallogr. D Biol. Crystallogr.* **66**, 12–21 (2010).
62. Abelev, B.I. *et al.* Longitudinal double-spin asymmetry for inclusive jet production in $\bar{p} + \bar{p}$ collisions at $\sqrt{s} = 200$ GeV. *Phys. Rev. Lett.* **100**, 232003 (2008).
63. Khalili-Araghi, F. *et al.* Calculation of the gating charge for the Kv1.2 voltage-activated potassium channel. *Biophys. J.* **98**, 2189–2198 (2010).
64. Klauda, J.B. *et al.* Update of the CHARMM all-atom additive force field for lipids: validation on six lipid types. *J. Phys. Chem. B* **114**, 7830–7843 (2010).
65. MacKerell, A.D. *et al.* All-atom empirical potential for molecular modeling and dynamics studies of proteins. *J. Phys. Chem. B* **102**, 3586–3616 (1998).
66. Jorgensen, W.L., Chandrasekhar, J., Madura, J.D., Impey, R.W. & Klein, M.L. Comparison of simple potential functions for simulating liquid water. *J. Chem. Phys.* **79**, 926–935 (1983).
67. Phillips, J.C. *et al.* Scalable molecular dynamics with NAMD. *J. Comput. Chem.* **26**, 1781–1802 (2005).
68. Shaw, D.E. *et al.* Anton, a special-purpose machine for molecular dynamics simulation. *Commun. ACM* **51**, 91–97 (2008).
69. Feller, S.E. & MacKerell, A.D. An improved empirical potential energy function for molecular simulations of phospholipids. *J. Phys. Chem. B* **104**, 7510–7515 (2000).
70. Humphrey, W., Dalke, A. & Schulten, K. VMD: visual molecular dynamics. *J. Mol. Graph.* **14**, 33–38, 27–28 (1996).

Erratum: Structural mechanism of voltage-dependent gating in an isolated voltage-sensing domain

Qufei Li, Sherry Wanderling, Marcin Paduch, David Medovoy, Abhishek Singharoy, Ryan McGreevy, Carlos A Villalba-Galea, Raymond E Hulse, Benoît Roux, Klaus Schulten, Anthony Kossiakoff & Eduardo Perozo
Nat. Struct. Mol. Biol.; doi:10.1038/nsmb.2768; corrected online 23 February 2014

In the version of this article initially published online, an incorrect affiliation was listed for Klaus Schulten. Klaus Schulten is affiliated with the Beckman Institute and Department of Physics, University of Illinois at Urbana-Champaign, Urbana, Illinois, USA. In addition, in Figure 5c, one of the structures was incorrectly labeled. Kv1.2 ch is shown in purple in the left panel of Figure 5c. The errors have been corrected for the print, PDF and HTML versions of this article.